

DETECTION OF COHERENT STRUCTURES IN PHOTOSPHERIC TURBULENT FLOWS

ABRAHAM C.-L. CHIAN^{1,2}, ERICO L. REMPEL^{1,3}, GUILLAUME AULANIER², BRIGITTE SCHMIEDER², SHAWN C. SHADDEN⁴, BRIAN T. WELSCH⁵, AND ANTHONY R. YEATES⁶

ABSTRACT

We study coherent structures in solar photospheric flows in a plage in the vicinity of the active region AR 10930 using the horizontal velocity data derived from Hinode/SOT magnetograms. Eulerian and Lagrangian coherent structures are detected by computing the Q-criterion and the finite-time Lyapunov exponents of the velocity field, respectively. Our analysis indicates that, on average, the deformation Eulerian coherent structures dominate over the vortical Eulerian coherent structures in the plage region. We demonstrate the correspondence of the network of high magnetic flux concentration to the attracting Lagrangian coherent structures (a-LCS) in the photospheric velocity based on both observations and numerical simulations. In addition, the computation of a-LCS provides a measure of the local rate of contraction/expansion of the flow.

Subject headings: Sun: photosphere — Sun: surface magnetism — turbulence

1. INTRODUCTION

The spatiotemporal patterns and transport of magnetic field in the photosphere are driven by the turbulent plasma flows in the solar convection zone. Solar magnetic fields are observed in complex and hierarchical structures covering a wide range of scales that emerge and vanish on the time-scales of turbulent convective patterns. Traditionally, they are classified by size and lifetime as patterns of granulation (1 Mm, 0.2 h), meso-granulation (5-10 Mm, 5 h) and supergranulation (15-35 Mm, 24 h). Recently, the idea is emerging that meso and supergranulation are signatures of a collective interaction of granular cells (Del Moro et al. 2007). The continuous restructuring of surface magnetic fields by photospheric turbulent flows plays a key role in determining the topology and evolution of chromospheric and coronal magnetic fields, and may influence the triggering of eruptive solar events such as flares, coronal mass ejections or sudden disappearance of filaments (Roudier et al. 2009). For example, Rondi et al. (2007) and Roudier et al. (2008) used space and ground observations to show that large-scale horizontal photospheric flows below and around a filament influence the formation and evolution of filaments, leading to destabilization of the coronal magnetic field.

Spectral line observations of the Sun with high spatial resolution show small-scale bright points, with widths $\lesssim 0.5$ Mm, located in the intergranular lanes. Bright points are associated with localized regions of strong

magnetic field and correspond to magnetic flux tubes of kilogauss field strength that stand nearly vertically in the solar atmosphere (Solanki 1993). Some bright points exhibit the proper motions of convectively driven vortical flows created at the downdrafts where the plasma follows spiral paths and returns to the solar interior after cooling down (Bonet et al. 2008). Recent balloon-borne Sunrise observations show 3.1×10^{-3} vortices $\text{Mm}^{-2} \text{min}^{-1}$, with a mean lifetime of 7.9 min and a standard deviation of 3.2 min (Bonet et al. 2010). These magnetized vortex tubes have been predicted by the theory of magnetoconvection (Brandenburg et al. 1996; Stein & Nordlund 1998) and observed in 3D radiative/compressible MHD simulations (Kitiashvili et al. 2010, 2012; Shelyag et al. 2011; Rempel et al. 2013). Photospheric vortex structures with high concentration of magnetic field provide an important path for energy and momentum transfer from the convection zone into the chromosphere (Kitiashvili et al. 2012) and may be relevant for chromospheric-coronal heating (van Ballegoijen et al. 1998; Hasan & van Ballegoijen 2008).

A number of observational and theoretical works have applied the Lagrangian approach to trace the flow of bright points and the pattern of the magnetic network. Simon et al. (1988) measured the horizontal flow field on the solar surface using the technique of local correlation tracking (LCT) on a 28 min time sequence of white-light images of the Solar Optical Universal Polarimeter instrument onboard the Spacelab2. They showed that insight into the relationship between flows and magnetic fields is acquired by calculating the flow of passive test particles, called “corks”, that are originally distributed uniformly in the flow field. The cork paths, representing the Lagrangian tracers of the pathlines of the flow, congregate at the same locations of the magnetic network. A simplified kinematic model of convection at the solar surface was developed by Simon & Weiss (1989) to interpret observations and predict the evolution of magnetic fields. They compared the cork patterns of the simulated flow with the cork patterns of the observed magnetic network,

abraham.chian@gmail.com
rempel@ita.br

¹ National Institute for Space Research (INPE), World Institute for Space Environment Research (WISER), P.O. Box 515, 12227-010 São José dos Campos – SP, Brazil

² Observatoire de Paris, LESIA, CNRS, 92190 Meudon, France

³ Institute of Aeronautical Technology (ITA), WISER, 12228-900 São José dos Campos – SP, Brazil

⁴ Department of Mechanical Engineering, University of California, Berkeley, CA 94720, USA

⁵ Space Science Laboratory, University of California, Berkeley, CA 94720, USA

⁶ Department of Mathematical Sciences, Durham University, Durham, DH1 3LE, UK

and discussed the extent to which magnetic flux tubes can be regarded as moving passively with the large-scale photospheric flow. van Ballegoijen *et al.* (1998) used the G-band images of the Swedish Vacuum Solar Telescope to show that bright points are arranged in linear structures, called “filigrees”, located in the lanes between neighboring granule cells and to measure the motion of bright points using an object tracking technique; comparison with a 2D simulation of horizontal motions of magnetic flux elements in response to solar granulation flows shows that the observed velocities and spatial distribution of the bright points are consistent with passive advection of corks by the solar granulation flow. Del Moro *et al.* (2007) reconstructed the 3D velocity field of a single supergranular cell from the spectrometer data of the Interferometric Bidimensional Spectrometer, and used the tracking of corks to show that a divergence structure is created by a compact region of constant up-flow close to the cell centre, and isolated regions of strong convergent down-flow are nearby or cospatial with extended clusters of bright CaII wing features forming the knots of the magnetic network. Schmieder *et al.* (2013) applied the coherent structure tracking (CST) algorithm to track granules and analyze large-scale photospheric flows related to an extended filament in the active region AR 11106 using the H_α image of the THEMIS telescope and the EUV imager (AIA) of Solar Dynamic Observatory. They showed that diverging flows inside the supergranules may be similar in and out of the filament channel. In addition, they identify converging flows, corresponding to accumulation of corks, around the footpoints or barbs located at the edges of the EUV filament. The frequent EUV brightenings suggest the occurrence of reconnections of the magnetic field lines of the flux tube with the environment at the convergence points at the edges of the EUV filament channel.

There is observational evidence of anomalous transport and turbulence in photospheric flows and magnetic fields. Schrijver *et al.* (1992) and Lawrence & Schrijver (1993) applied the percolation theory to report sub-diffusion of magnetic elements in the photosphere. Cadavid *et al.* (1999) used a 70 min sequence of G-band image of the Swedish Vacuum Solar Telescope on 5-October-1995 to show that the transport of bright points near the disk center is subdiffusive due to the trapping of walkers at the stagnation points in the fractal intercellular pattern; the distribution of waiting times at the trap sites obeys a Lévy (power-law) distribution. Lawrence *et al.* (2001) applied subsonic filtering to the data of Cadavid *et al.* (1999) to report super-diffusion and show that the spatiotemporal scaling of the bright point dynamics indeed indicates the presence of turbulence in the intergranular lanes. Lawrence *et al.* (2011) used a 32 min sequence of G-band and Ca II K-line intensity measurements of the Dunn Solar Telescope on 28-May-2009, at the disk center of size $32 \text{ Mm} \times 32 \text{ Mm}$, to investigate high-frequency fluctuations in both photosphere and chromosphere; their noise-corrected G-band spectrum for $f = 28 - 326 \text{ MHz}$ shows a power law with exponent -1.21 ± 0.02 , consistent with the presence of turbulent motions. Moreover, they showed that the G-band spectral power in the 25-100 MHz range is concentrated at the locations of magnetic bright points in the intergranular lanes and is highly intermittent in time,

being characterized by a positive kurtosis, which implies that the fluctuations have non-Gaussian probability distribution functions (PDF) with broad tails indicative of turbulence. Cadavid *et al.* (2012) showed that the noise-filtered power spectrum of the Hinode/SOT data with a sequence of 80 min on 5-March-2007, in the internetwork near the Sun center of size $20 \text{ Mm} \times 20 \text{ Mm}$, presents a scaling range of $32 < f < 53 \text{ MHz}$ with characteristic power law exponents of -1.56 for G-band and of -4.00 for H-line, confirming the presence of turbulent fluctuations. By integrating the Hinode/SOT G-band spectra in the range 32-53 MHz, they identified the sites of increased G-band power with the location of G-band bright points. Abramenko *et al.* (2011) and Lepreti *et al.* (2012) used the images of New Solar Telescope of Big Bear Solar Observatory to report super-diffusion and turbulent pair dispersion of bright points in active region plage, quiet-sun, and coronal hole.

The aim of this paper is to apply Eulerian and Lagrangian tools to detect coherent structures in images of photospheric turbulent flows. First, we apply the Eulerian approach to compute the Q-criterion and distinguish regions of the plasma flow dominated by the deformation and vortical coherent structures (Hunt *et al.* 1988). Next, we apply the tool of Lagrangian coherent structures (LCS) to determine the repelling and attracting material lines that organize the transport of plasma flow. The term “Lagrangian” refers to flows defined by the fluid motion instead of an instantaneous snapshot (Eulerian); the term “coherent” refers to the distinguished stability of these structures compared to other nearby material lines/surfaces. There is a growing interest to adopt the LCS approach (Haller & Yuan 2000; Shadden 2011) to improve the understanding of transport in complex flows such as planetary atmosphere (Sapsis & Haller 2009; Peng & Peterson 2012), oceans (Beron-Vera *et al.* 2010; Lehahn *et al.* 2011), and cardiovascular system (Shadden & Taylor 2008; Arzani & Shadden 2012). A number of papers have studied LCS in complex plasma flows for thermonuclear applications (Leoncini *et al.* 2006; Padberg *et al.* 2007; Borgogno *et al.* 2011) and astrophysical applications (Rempel *et al.* 2011, 2012, 2013; Yeates *et al.* 2012). In this paper, we apply the backward finite-time Lyapunov exponents (b-FTLE) to study the attracting LCS of the photospheric turbulence. We show that, like the “corks”, the b-FTLE is able to trace the patterns of the magnetic network. Moreover, it gives a quantitative measure of the local rate of contraction/expansion of the photospheric flow.

2. THE HORIZONTAL VELOCITY DATA

Our study is based on a 12 h high-resolution sequence of velocity images (cadence $\sim 121 \text{ s}$) of photospheric flow derived from the Hinode-SOT magnetograms, from 12-Dec-2006 14:24 UT to 13-Dec-2006 02:24 UT, by selecting a unipolar plage area of size $12.4 \text{ Mm} \times 12.4 \text{ Mm}$ ($\sim 17'' \times 17''$) near the active region AR 10930 (Yeates *et al.* 2012). The horizontal velocity field is a “proxy” extracted from the line-of-sight magnetic field (B_z) using the Fourier local correlation tracking method (FLCT) (Welsch *et al.* 2004, 2012).

It is worth pointing out that there are uncertainties in the correlation tracking that do not fully resolve the velocity fields in either space or time. The detailed descrip-

tion of the data reduction procedure is given in Welsch et al. (2012) and Yeates et al. (2012). The FLCT method involves a number of optimum parameters which are determined by an autocorrelation analysis in order to maximize frame-to-frame correlations and ensure robustness in the velocity estimate. In view of the reduction of noise by averaging in the tracking procedure, the actual velocity patterns of the photospheric flow might be more complicated than the “proxy”.

Yeates et al. (2012) showed that the build-up of magnetic gradients in solar corona can be inferred directly from the photospheric velocity data, without recourse to magnetic field extrapolation. They established the correspondence of the network of quasi-separatrix layers (Démoulin et al. 1996) to the repelling LCS in the photospheric velocity. In this paper, we extend the analysis of Yeates et al. (2012) to establish the correspondence of the network of high magnetic flux concentration to the attracting LCS in the photospheric velocity.

3. EULERIAN COHERENT STRUCTURES IN THE PHOTOSPHERE

Eulerian coherent structures can be extracted from the velocity field by computing the Q -criterion, also known as the Okubo-Weiss parameter in 2D turbulence (Hunt et al. 1988),

$$Q = \frac{1}{2} [|\Omega|^2 - |S|^2], \quad (1)$$

where the Frobenius matrix norm is adopted and S and Ω are defined by the decompositions of the gradient tensor of the velocity field

$$\nabla u = S + \Omega, \quad (2)$$

and

$$S = \frac{1}{2} [\nabla u + (\nabla u)^\top], \quad \Omega = \frac{1}{2} [\nabla u - (\nabla u)^\top], \quad (3)$$

where \top denotes the transpose of a tensor. The strain-rate (or deformation) tensor S is the symmetric part of ∇u ; its eigenvectors form an orthonormal set along the principle directions of fluid element deformation caused by tension, and its eigenvalues are real quantities that measure the rates of deformation in the corresponding directions. The vorticity tensor Ω is the anti-symmetric part of ∇u . For example, the deformation calculated using the Ulysses data shows that the magnetic tension causes local stretching of solar wind plasma elements mostly along the direction of the average magnetic field, whereas the solar wind vorticity tends to become perpendicular to the mean radial direction at large heliospheric distances (Polygiannakis et al. 1996).

Snapshot images of Eulerian coherent structures of the horizontal velocity field detected by Hinode in a plage region near AR 10930 (Yeates et al. 2012) are shown in Figure 1 for four instances: 12-Dec-2006 14:24 UT, 12-Dec-2006 18:24 UT, 12-Dec-2006 22:24 UT, 13-Dec-2006 02:24 UT. The first column shows magnetograms; the second column depicts the streamlines computed using the method of line integral convolution, which displays the integral curves of (u_x, u_y) in different tones of orange; some vortex coherent structures (patches) can

be visualized in these plots. The third column depicts the (x, y) plots of the deformation Eulerian coherent structures, which are identified by the localized patches with high values of $|S|^2$. The fourth column depicts the (x, y) plots of the vortical Eulerian coherent structures, which are identified by the localized patches with high values of $|\Omega|^2$. The average spatial size and lifetime of these vortices are similar to the magnetic bright points observed by Bonet et al. (2008, 2010). The fifth column depicts the (x, y) plots of the Q -criterion given by Eq. (1), which partitions the turbulent flow into the deformation-dominated ($Q < 0$, blue patches) and vorticity-dominated ($Q > 0$, red patches) regions.

The intensity of a turbulent flow is characterized by the magnitude of the root-mean-squared velocity fluctuations, deformation, and vorticity (Steinberg & Driscoll 2009). The probability distribution functions (PDF) of Eulerian coherent structures, associated with Figure 1, are shown in Figure 2. Some trends are evident. Figures 2(a) and 2(b) show that there are higher (lower) statistics for the low (high) values of the magnitudes of deformation and vorticity. Figure 1(c) shows that for all four instances the Q -criterion is distributed amongst negative and positive values, with non-Gaussian PDF. Note that the PDF of the Q -criterion shows a strong asymmetry skewed towards negative values, which indicates that in the plage region under study the photospheric turbulent flow is dominated by the strain-rate field. This situation is similar to a laboratory experiment of the turbulence-flame interaction, where the flame surface straining is dominated by the deformation whereas the role of the vorticity is to curve the flame surface creating wrinkles (Steinberg & Driscoll 2009).

The mean values of Eulerian coherent structures for four instances are summarized in Table 1. It confirms the features of PDF seen in Figure 2, i.e., in the plage region under study, on average: (i) the deformation dominates over the vorticity, (ii) the Q -criterion shows negative values implying the dominance of the deformation coherent structures over the vortical coherent structures.

TABLE 1
MEAN VALUES OF THE EULERIAN COHERENT STRUCTURES

	$\langle S ^2 \rangle$	$\langle \Omega ^2 \rangle$	$\langle Q \rangle$
12-Dec-2006 14:24 UT	5.0453e-08	1.8139e-08	-1.6157e-08
12-Dec-2006 18:24 UT	7.3680e-08	2.4142e-08	-2.4769e-08
12-Dec-2006 22:24 UT	8.0154e-08	2.2815e-08	-2.8670e-08
13-Dec-2006 02:24 UT	4.9614e-08	1.4840e-08	-1.7387e-08

Although the deformation and vortical coherent structures can be extracted by the Eulerian technique using the Q -criterion, it relies on instantaneous snapshots of the velocity field. In the next section we show that the transport barriers in the turbulent flow can be detected with greater precision by the technique of LCS.

4. LAGRANGIAN COHERENT STRUCTURES IN THE PHOTOSPHERE

Analogous to “corks” discussed in Section 1, the finite-time Lyapunov exponent (FTLE) can be computed by advecting a dense grid of tracer particles over the domain of interest. Consider a passive particle advected by the velocity field $\mathbf{u}(\mathbf{r}, t)$ from an initial time t_0 . We use the

horizontal velocity field derived from the Hinode SOT data for the plage region of Figure 1 to solve the particle advection equation

$$\frac{d\mathbf{r}}{dt} = \mathbf{u}(\mathbf{r}, t), \quad \mathbf{r}(t_0) = \mathbf{r}_0, \quad (4)$$

over a grid of initial positions \mathbf{r}_0 until the final positions $\mathbf{r}(t_0 + \tau)$ are reached after a finite integration time τ . The particle trajectories are obtained by a fourth-order Runge-Kutta integrator with cubic spline interpolation in both space and time. The finite-time Lyapunov exponents of the particle trajectories for a 2D flow are calculated at each initial position \mathbf{r}_0 as (Shadden *et al.* 2005; Shadden 2011; Rempel *et al.* 2011, 2012, 2013; Yeates *et al.* 2012)

$$\sigma_i^{t_0+\tau}(\mathbf{r}_0) = \frac{1}{|\tau|} \ln \sqrt{\lambda_i}, \quad i = 1, 2, \quad (5)$$

where λ_i ($\lambda_1 > \lambda_2$) are the eigenvalues of the finite-time right Cauchy-Green deformation tensor $\Delta = J^\top J$, $J = d\phi_{t_0}^{t_0+\tau}(\mathbf{r})/d\mathbf{r}$ is the deformation gradient, \top denotes the transpose and $\phi_{t_0}^{t_0+\tau} : \mathbf{r}(t_0) \rightarrow \mathbf{r}(t_0 + \tau)$ is the flow map for Eq. (4). In forward time ($\tau > 0$), the maximum FTLE, σ_1 , gives the finite-time average of the maximum rate of either divergence (if $\sigma_1 > 0$) or convergence (if $\sigma_1 < 0$) between the trajectories of a fiducial particle at \mathbf{r} and its neighboring particles. The maximum stretching is found when the neighboring particle \mathbf{s} is such that $\xi_0 = \mathbf{r}_0 - \mathbf{s}$ is initially aligned with the eigenvector of Δ associated with $\lambda_1 > 0$. If two points are initially separated by a small distance $|\xi_0|$ at time t_0 , then their maximum separation at a later time t_1 will be $|\xi_1| \sim \exp[\sigma_1^{t_1}(\mathbf{r}_0)|t_1 - t_0|]|\xi_0|$. σ_2 provides information about stretching/contraction in another direction and can be useful to interpret the local dynamics of the fluid. Local minima in the maximum forward finite-time Lyapunov exponent (f-FTLE) provides a way to detect the position of the center of vortices in the velocity field since vortices may be viewed as material tubes of low particle dispersion. In backward time ($\tau < 0$), $\sigma_1 > 0$ represents regions of the flow with convergence and $\sigma_1 < 0$, regions with divergence of nearby trajectories.

Advecting a particle forward in time reveals the repelling LCS in the f-FTLE field, which are the source of stretching in the flow, whereas advecting a particle backward in time reveals the attracting LCS in the b-FTLE field along which particles congregate to form the observable patterns (Sapsis & Haller 2009). The properties of an LCS depend on the choice of the integration time τ , which should be chosen long enough for dominant features to be revealed, yet short enough for the FTLE to be representative of the transient dynamics of interest.

Three examples of repelling LCS for the photospheric turbulent flow in the plage region under study are given in Figures 3(a)-(c), which show the maximum f-FTLE σ_1 computed by solving the particle advection equation (4) from the initial time $t_0 = 12\text{-Dec-2006 } 14:24 \text{ UT}$ to the final time $t_0 + \tau$, with $\tau = +4\text{h}$ (Figure 3(a)), $+8\text{h}$ (Figure 3(b)), and $+12\text{h}$ (Figure 3(c)), respectively. Thin ridges of large (positive) f-FTLE in Figures 3(a)-(c) represent the locally strongest repelling material lines in the photospheric flow, which confirm the results of Yeates *et al.*

(2012) using $\tau = +6\text{h}$ and $+12\text{h}$. As we increase integration time we notice some structures persist and become more sharply defined. These structures can be considered most influential over time. The structures that fail to persist as integration time is increased can be considered to be due to more transient flow features.

Three examples of attracting LCS for the photospheric turbulent flow in the plage region under study are given in Figures 3(d)-(f), which show the maximum b-FTLE σ_1 computed by solving the particle advection equation (4) from the initial time $t_0 = 13\text{-Dec-2006 } 02:24 \text{ UT}$ to the final time $t_0 + \tau$, with $\tau = -4\text{h}$ (Figure 3(d)), -8h (Figure 3(e)), and -12h (Figure 3(f)), respectively. Thin ridges of large (positive) b-FTLE in Figures 3(d)-(f) represent the locally strongest attracting material lines in the photospheric flow.

In order to illustrate the temporal evolution of LCS, we compute the forward- and backward-time FTLE of the photospheric velocity field at $t_0 = 12\text{-Dec-2006 } 18:24 \text{ UT}$ and $t_0 = 12\text{-Dec-2006 } 22:24 \text{ UT}$, using the same integration time $|\tau| = 4\text{h}$. Figure 4 displays the repelling (green) and attracting (red) LCS for two t_0 , which form the ‘‘Lagrangian skeletons’’ of the photospheric turbulence.

Attracting and repelling LCS act as barriers to particle transport. A material line is a smooth curve of fluid particles advected by the velocity field (Haller 2001). These attracting and repelling material lines are the analogous of stable and unstable manifolds of time-independent fields (Shadden *et al.* 2005; Shadden 2011). Numerical studies of 2D flows have elucidated the role of material lines (Haller & Yuan 2000; Miranda *et al.* 2013). Consider a steady flow, where the velocity field does not change with time. In the presence of counter-rotating vortices, hyperbolic (saddle) points are expected to be found. The trajectories of passive scalars follow the velocity vectors in the vicinity of the hyperbolic point. Thus, particles lying on the stable manifold are attracted to the saddle point in the forward-time dynamics and trajectories on the unstable manifold converge to the saddle point in the backward-time dynamics (Rempel *et al.* 2012). Two particles are said to straddle a manifold if the line segment connecting them crosses the manifold. The maximum FTLE typically has high values on the stable manifold in forward-time, since nearby trajectories straddling the manifold will experience exponential divergence when they approach the saddle point. Similarly, the FTLE field exhibits a local maximizing curve (ridge) along the unstable manifold in backward-time dynamics, since trajectories straddling the unstable manifold diverge exponentially when they approach the saddle point in reversed-time. Thus, ridges in the forward-time FTLE field mark the stable manifolds of hyperbolic points and ridges in the backward-time FTLE field mark the unstable manifolds. Analogously, for a time-dependent velocity field, regions of maximum material stretching generate ridges in the FTLE field. Thus, the repelling material lines (finite-time stable manifolds) produce ridges in the maximum FTLE field in the forward-time system and attracting material lines (finite-time unstable manifolds) produce ridges in the backward-time system, as seen in Figures 3 and 4.

In this paper, we showed that Eulerian coherent structures and Lagrangian coherent structures give very different information of the dynamics and structure of astrophysical plasma flows. Eulerian coherent structures give instantaneous information of plasma dynamics and structure at a given time, whereas Lagrangian coherent structures account for the integrated effect of plasma dynamics and structure in a finite-time interval. Arguably, instantaneous quantities may be considered inappropriate to understand inherently transient phenomenon since such quantities may not properly convey the integrated behavior of constantly changing flow. LCS typically account for such integrated behavior more naturally by considering the integrated fluid motion to reveal organizing flow features.

In the context of photospheric turbulence, we showed in Figure 1 that the Eulerian analysis is able to differentiate two types of coherent structures arising from either deformation or vorticity. An enlargement of the rectangle region indicated at Figure 1 at 12-Dec-2006 18:24 UT is depicted in Figure 5. The pattern of streamlines in Figure 5(a) identifies the localized region of a vortex in the photospheric flow. Figures 5(c) and 5(d) show that this vortex region is characterized by high values of the modulus of both deformation and vorticity. Figure 5(b) shows that the Q-criterion can differentiate clearly two subregions: one being the deformation Eulerian coherent structures (blue subregion) and the other being the vortical Eulerian coherent structures (red subregion). For the sake of clarity, a corresponding 3D view of Figure 5 is presented in Figure 6. Our Eulerian analysis shows that, on average, in the plage region the deformation Eulerian coherent structures dominate over the vortical Eulerian coherent structures in the turbulent photospheric flows, as seen in Figure 2.

The Lagrangian analysis is able to provide further information of magnetic and velocity fields of the photospheric turbulence missing in the Eulerian analysis. Yeates et al. (2012) demonstrated that it is possible to make the link between the squashing Q-factor and the maximum Lyapunov exponent σ_1 of the repelling Lagrangian coherent structures, since both quantities are similar measures of the local rate of stretching at a given point and defined by the norm of the Cauchy-Green tensor of the deformation imposed by the field-line mapping. Note, however, that there are some differences between these two quantities. While the squashing Q-factor uses the Frobenius norm of the tensor, σ uses the spectral norm; while the squashing Q-factor is dimensionless, σ has units of inverse time and includes the logarithm in its definition in Eq. (5). The close similarity of these two quantities is shown in Figure 7, where the squashing Q-factor calculated for the same region of the photosphere under study is shown in Figure 7(a) and the corresponding repelling Lagrangian coherent structures are shown in Figure 7(b). Both Figures 7(a) and 7(b) are computed for $t_0 = 12\text{-Dec-2006 } 14:24 \text{ UT}$ and $\tau = +12 \text{ h}$, the same as Figure 3(c). Figure 7(a) adopts the logarithmic scaling since certain trajectories typically become exponentially separated in time, which shows the emergence of thin ridges of high values of the squashing Q-factor representing the quasi-separatrix layers. These ridges are interspersed by regions of low values of the squashing Q-factor. Figure 7(b) shows the emergence

of thin ridges of high positive values of σ_1 , representing the locally strongest repelling material surfaces in the photospheric flow. These ridges are interspersed by regions of negative σ_1 that represent converging trajectories of the plasma transport. Evidently, the ridges of the quasi-separatrix layers in Figure 7(a) are co-spatial with the ridges of the photospheric flow in Figure 7(b). For the sake of clarity, a 3D view of the rectangle regions of Figure 7 is presented in Figure 8. Note that the spiky features seen in Figure 8(a) may be related to numerical issues which can be smoothed by applying a refined numerical procedure (Partiat & Démoulin 2012).

As mentioned in Section 1, the Lagrangian analysis based on corks can provide insight into the relationship between magnetic fields and plasma flows in the photosphere. Roudier et al. (2009) used a 48 h time sequence of the horizontal velocity data from the Solar Optical Telescope (SOT) onboard Hinode to study the interactions between granular to supergranular scales in a quiet region of the photosphere. They showed that the tree of fragmenting granules plays a crucial role in the advection of the magnetic field and in the build-up of the magnetic network. In particular, the long time sequence of their analysis shows that the trajectory of plasma flows traced by corks matches exactly the position of the highest magnetic flux concentration of the network, which lies on supergranule boundaries. Our technique of Lagrangian coherent structures is closely related to corks, but gives additional important information missing in the cork-based studies as demonstrated below. Figure 9 shows a comparison of the line-of-sight magnetic field B_z measured by Hinode/SOT at $t = 13\text{-Dec-2006 } 02:24 \text{ UT}$ (Figure 9(a), same as Figure 1) and the attracting Lagrangian coherent structures computed for $t_0 = 13\text{-Dec-2006 } 02:24 \text{ UT}$ and $\tau = -12 \text{ h}$ (Figure 9(b), same as Figure 3(f)). It is possible to identify similar patterns in Figures 9(a) and 9(b). For example, a superposition of the rectangle regions marked in Figures 9(a)-(b) is shown in Figure 9(c) (where the thresholded b-FTLE with $\sigma_1 > 4 \times 10^{-5}$ is plotted) that shows clearly the proximity of the trajectory of plasma flows to the magnetic field, similar to the cork results of Roudier et al. (2009). In addition, Figure 9(b) shows the emergence of thin ridges of high positive values of σ_1 , representing the locally strongest attracting material surfaces in the photospheric flow. These ridges are interspersed by regions of negative σ_1 that represent diverging trajectories of the plasma transport. For the sake of clarity, a 3D view of the rectangle regions of Figure 9 is presented in Figure 10.

In order to confirm the validity of Figures 9 and 10, we performed 3D numerical simulations of large-scale dynamos in turbulent compressible convection with uniform horizontal shear and rotation. The dimensionless compressible magnetohydrodynamics equations are solved in a simulation box divided into three layers, an upper cooling layer, a convectively unstable layer, and a stable overshoot layer, with constant gravity in the vertical direction, as described by Käpylä et al. (2008). The box has dimensions $(L_x, L_y, L_z) = (8, 8, 2)d$, where d is the depth of the convectively unstable layer, and shearing periodic boundary conditions are used in the horizontal direction. In the vertical direction we use stress-free boundary con-

ditions for the velocity field and vertical field conditions for the magnetic field. In our simulations we adopt dimensionless quantities, setting $d = \rho_0 = g = \mu_0 = 1$, where g is gravity, distance is in units of d , density in units of the initial value at the base of convective layer ρ_0 , time in units of the free fall time $\sqrt{d/g}$, velocity in units of \sqrt{dg} and magnetic field in units of $\sqrt{d\rho_0\mu_0g}$.

The physical parameters (e.g. kinematic viscosity, resistivity, heat conductivity, rotation velocity, etc.) are chosen to ensure the onset of a large-scale magnetic field in a moderately turbulent velocity field. For a detailed setup, we direct the reader to run D2 in Käpylä *et al.* (2008). The model is solved with the PENCIL CODE⁷, which employs sixth-order finite-differences in space and third-order variable step Runge-Kutta integration in time.

Figure 11(a) shows a 2D image of the vertical component of the magnetic field B_z near the top of the convective layer at a time t_0 when the magnetic energy growth has already saturated. This figure shows that the simulated large-scale turbulent dynamo reproduces the pattern of convective cells, similar to granulations in the photosphere. In particular, it shows that the network of high concentration of magnetic flux is located in the boundaries between the convective cells, corresponding to the intergranular lanes. The elongated convective cells in Figure 11 result from the shear. Since there is an imposed large-scale flow in the y direction, it is expected that the convective cells would be elongated along this direction. This is more pronounced after a strong large-scale magnetic field develops due to the dynamo mechanism. Figure 11(b) shows the b-FTLE computed for the horizontal velocity field (v_x, v_y) at t_0 using $\tau = -10$ time units. The ridges of high values of b-FTLE in Figure 11(b) indicate the locations of converging plasma flows. In Figure 11(c) we plot the superposition of the thresholded b-FTLE (with $\sigma_1 > 0.1$) on top of B_z . For the sake of clarity, a 3D view of the rect-

angle regions of Figure 11 is given in Figure 12, where the modulus of B_z is plotted in comparison with the b-FTLE. Evidently, Figures 11 and 12 render support for the results of Figures 9 and 10 that there is correspondence of the network of high magnetic flux concentration to the attracting LCS in the photospheric velocity.

In conclusion, we extended the observational study by Yeates *et al.* (2012) of Lagrangian coherent structures in the photospheric velocity to show that in addition to the correspondence of the network of quasi-separatrix layers in the repelling LCS demonstrated by Yeates *et al.* (2012), there is a correspondence of the network of high magnetic flux concentration to the attracting LCS in the photospheric flows, confirmed by both observations and numerical simulations. Hence, the repelling and attracting LCS of the photospheric velocity provide complementary informations of the local dynamics and topology of solar magnetic fields. Although the corks coincide with the network of magnetic flux, they are not the best way to find the transport barriers and the directions of the flow convergence. We showed that the attracting LCS are more suitable for these tasks because they trace continuous curves (material lines) that are the explicit structures potentially responsible for observed physical patterns and at the same time measure the local rate of contraction/expansion in the flow. While Eulerian coherent structures provide useful insights of the snapshot of the photospheric flows, they fail to reveal the fine structures of the transport barriers and the local dynamics of the flows that are readily provided by the repelling and attracting Lagrangian coherent structures.

A.C.L.C. acknowledges the support of CNPq, the award of a Marie Curie Fellowship by the European Commission, and the hospitality of Paris Observatory. ELR acknowledges the financial support of CNPq (Brazil) and FAPESP (Brazil). We thank Petri Käpylä for providing the configuration files for the PENCIL CODE MHD simulations.

REFERENCES

- Abramenko, V. I., Carbone, V., Yurchyshyn, V., Goode, P. R., Stein, R. F., Lepreti, Capparelli, V., & Vecchio, A. 2011, *ApJ*, 743, 133
- Arzani, A., & Shadden, S. C. 2012, *Phys. Fluids*, 24, 081901 [DOI: 10.1063/1.4744984]
- Balsara, D. S. & Kim, J. 2005, *ApJ*, 634, 390
- Beron-Vera, F. J., Olascoaga, M. J., & Goni, G. J. 2010, *J. Phys. Oceanography*, 40, 2466
- Bonet, J. A., Márquez, I., Sánchez Almeida, J., Cabello, I., & Domingo, V. 2008, *ApJ*, 687, L131
- Bonet, J. A., Márquez, I., Sánchez Almeida, J., *et al.* 2010, *ApJ*, 723, L139
- Brandenburg, A., Jennings, R. L., Nordlund, Å., *et al.* 1996, *J. Fluid Mech.*, 306, 3
- Borgogno, D., Grasso, D., Pegoraro, F., & Schep, T. J. 2011, *Phys. Plasma*, 18, 102307 [DOI: 10.1063/1.3647339]
- Cadavid, A. C., Lawrence, J. K., & Ruzmaikin, A. A. 1999, *ApJ*, 521, 844
- Cadavid, A. C., Lawrence, J. K., Christian, D. J., Jess, D. B., & Mathioudakis, M. 2012, in “Magnetic Fields from the Photosphere to the Corona”, T. R. Rimmele, M. Collados Vera, *et al.* (Eds.), ASP Conf. Series, Vol. 463, pp. 75-82
- Cattaneo, F., Hughes, D., & Kim, E. 1996, *Phys. Rev. Lett.*, 76, 2057
- Del Moro, D., Giordano, S., & Berrilli, F. 2007, *A&A*, 472, 599 [DOI: 10.1051/0004-6361:20077595]
- Démoulin, P., Henoux, J. C., Priest, E. R., & Mandrini, C. H. 1996, *A&A*, 308, 643
- Haller, G. 2001, *Physica D*, 149, 248
- Haller, G., & Yuan, G. 2000, *Physica D*, 147, 352
- Hasan, S. S., & van Ballegoijen, A. A. 2008, *ApJ*, 680, 1542
- Hunt, J. C. R., Wray, A. A., & Moin, P. 1988, Eddies, streams, and convergence zones in turbulent flows. Center for Turbulence Research Report CTR-S88, <http://ctr.stanford.edu/Summer/201306111537.pdf>
- Käpylä, P. J., Korpi, M. J., & Brandenburg, A. 2008, *A&A* 491, 353
- Kitiashvili, I. N., Kosovichev, A. G., Wray, A. A., & Mansour, N. N. 2010, *ApJ*, 719, 307
- Kitiashvili, I. N., Kosovichev, A. G., Mansour, N. N., & Wray, A. A. 2012, *ApJ*, 751, L21
- Lawrence, J. K., & Schrijver, C. J. 1993, *ApJ*, 411, 412
- Lawrence, J. K., Cadavid, A. C., Ruzmaikin, A. A., & Berger, T. E. 2001, *Phys. Rev. Lett.*, 86, 5894
- Lawrence, J. K., Cadavid, A. C., Christian, D. J., Jess, D. B., & Mathioudakis, M. 2011, *ApJ*, 743, L24
- Lehahn, Y., d’Ovidio, F., Lévy, M., Amitai, Y., & Eyal Heifetz, E. 2011, *Geophys. Res. Lett.*, 39, L16610 [DOI: 10.1029/2011GL048588]

⁷ <http://pencil-code.googlecode.com/>

- Leoncini, X., Agullo, O., Muraglia, M., & Chandre, C. 2006, *Eur. Phys. J. B*, 53, 351 [DOI: 10.1140/epjb/e2006-00390-7]
- Lepreti, F., Carbone, V., Abramenko, V. I., Yurchyshyn, V., P. R. Goode, P. R., Capparelli, V., Vecchio, A. 2012, *ApJ*, 759, L17 [DOI: 10.1088/2041-8205/759/1/L17]
- Miranda, R. A., Rempel, E. L., Chian, A. C.-L., Seehafer, N., Toledo, B. A., & Muñoz, P. R. 2013, *Chaos*, 23, 033107 [DOI: 10.1063/1.4811297]
- Padberg, K., Hauff, T., Jenko, F., & Junge, O. 2007, *New J. Phys.*, 9, 400 [DOI: 10.1088/1367-2630/9/11/400]
- Pariat, E., & Démoulin, P. 2012, *A&A*, 541, A78 [DOI:10.1051/0004-6361/201118515]
- Peng, J., & Peterson, R. 2012, *Atmospheric Environment*, 48, 230
- Polygiannakis, J. M., & Moussa, X. 1996, *Solar Phys.*, 166, 423
- Reyl, C., Antonsen, Jr., T. M., & Ott, E. 1996, *Phys. Plasmas*, 3, 2564
- Rempel, E.L., Proctor, M. R. E., & Chian, A.C.-L. 2009, *MNRAS*, 400, 509 [DOI: 10.1111/j.1365-2966.2009.15483.x]
- Rempel, E.L., Chian, A.C.-L., & Brandenburg, A. 2011, *ApJ*, 735, L9 [DOI: 10.1088/2041-8205/735/1/L9]
- Rempel, E.L., Chian, A.C.-L., & Brandenburg, A. 2012, *Phys. Scr.*, 86, 018405 [DOI: 10.1088/0031-8949/86/01/018405]
- Rempel, E. L., Chian, A.C.-L., Brandenburg, A., P. R. Muñoz, & Shadden, S. C. 2013, *J. Fluid Mechanics*, 729, 309 [doi:10.1017/jfm.2013.290]
- Rondi, S., Roudier, Th., Molodij, G., Bommier, V., Keil, S., Stüterling, P., Malherbe, J. M., Meunier, N., Schmieder, B., & Maloney, P. 2007, *A&A*, 467, 1289 [DOI: 10.1051/0004-6361:20066649]
- Roudier, T., Svanda, M., Meunier, N., Keil, S., Rientord, M., Malherbe, J. M., Rondi, S., Molodij, G., Bommier, V., & Schmieder, B. 2008, *A&A*, 480, 255 [DOI: 10.1051/0004-6361:20077973]
- Roudier, Th., Rieutord, M., Brito, D., Rincon, F. Malherbe, J. M., Meunier, N., Berger, T., & Frank, Z. 2009, *A&A*, 495, 945 [DOI: 10.1051/0004-6361:200811101]
- Sapsis, T., & Haller, G. 2009, *J. Atmos. Sci.*, 66, 2481
- Schmieder, B., Roudier, T., Mein, N., Mein, P., Malherbe, J. M., & Chandra, R. 2013, *A&A*, submitted
- Schrijver, C. J., Zwaan, C., Balke, A. C., Tarbell, T. D., Lawrence, J. K. 1992, *A&A*, 253, L1
- Shadden, S. C. 2011, *Lagrangian coherent structures, in Transport and Mixing in Laminar Flows; From Microfluids to Oceanic Currents*, edited by R. Grigoriev (Germany, Wiley VCH), Chap. 3
- Shadden, S. C. Lekien, F., & Marsden, J. e. 2005, *Physica D*, 212, 271
- Shadden, S. C., & Taylor, C. A. 2008, *Annals Biomedical Eng.*, 36, 1152 [DOI: 10.1007/s10439-008-9502-3]
- Shelyag, S., Keys, P., Mathioudakis, M. & Keenan, F. P. 2011, *A&A*, 526, A5 [DOI: 10.1051/0004-6361/201015645]
- Simon, G. W., Title, A. M., Topka, K. P., Tarbell, T. D., Shine, R. A., Ferguson, S. H., & Zirin, H. and SOUP Team 1988, *ApJ*, 327, 964
- Simon, G. W., & Weiss, N. O. 1989, *ApJ*, 345, 1060
- Solanki, S. 1993, *Space Sci. Rev.*, 63, 1
- Steinberg, A. M., & Driscoll, J. F. 2009, *Combustion Flame*, 156, 2285
- Stein, R. F., & Nordlund, A. 1998, *ApJ*, 499, 914
- van Ballegooijen, A. A., Nisenson, P., Noyes, R. W., Löfdahl, M. G., Stein, R. F., Nordlund, A., & Krishnakumar, V. 1998, *ApJ*, 509, 435
- Welsch, B. T., Fisher, G. H., Abbett, W. P., & Regnier, S. 2004, *ApJ*, 610, 1148
- Welsch, B. T., Kusano, K., Yamamoto, T. T., & Muglach, K. 2012, *ApJ*, 747, 130 [DOI: 10.1088/0004-637X/747/2/130]
- Yeates, A.R., Hornig, G., & Welsch, B.T. 2012, *A&A*, 539, A1 [DOI: 10.1051/0004-6361/201118278]
- Zienicke, E., Politano, H., & Pouquet, A. 1998, *Phys. Rev. Lett.*, 81, 4640

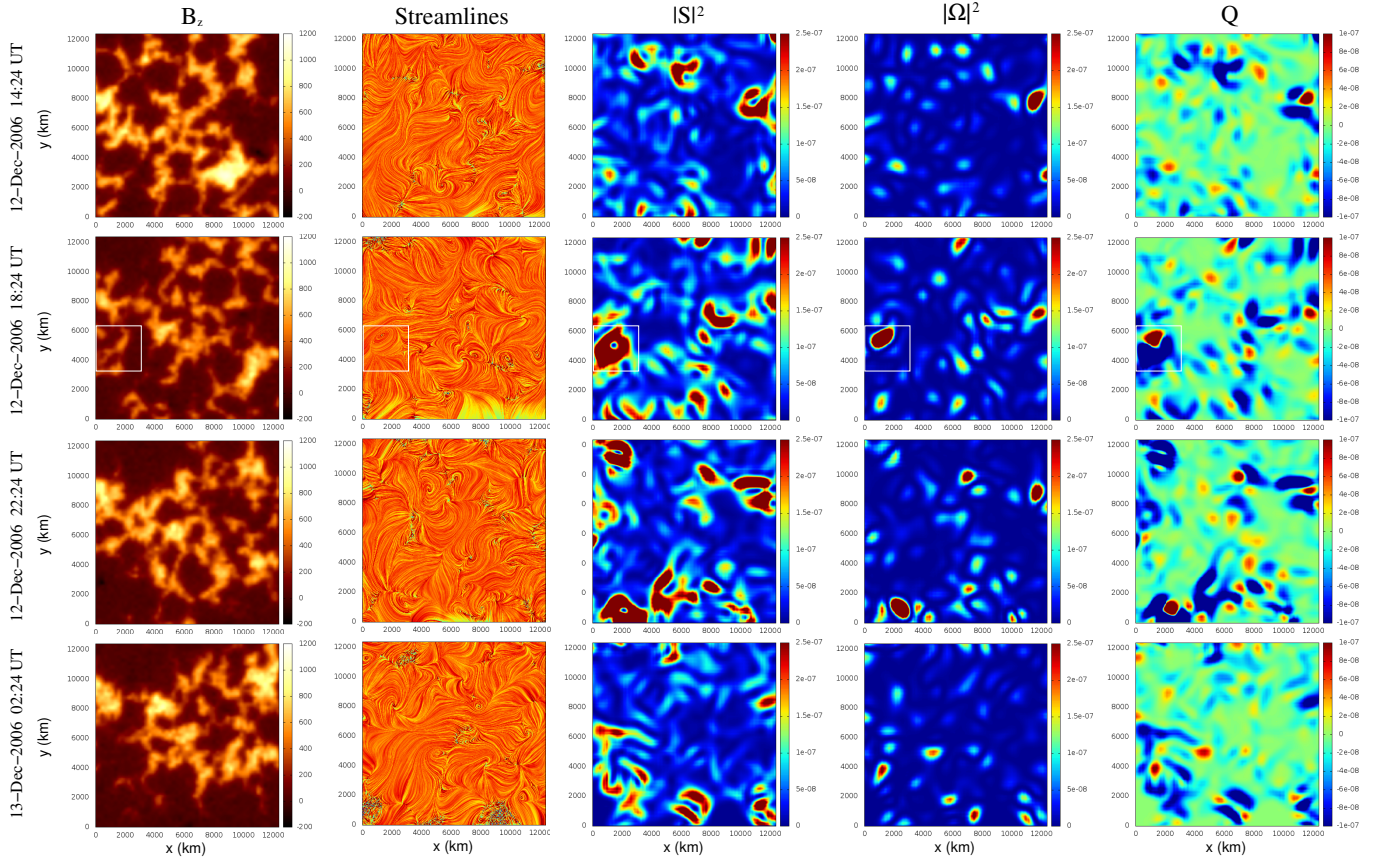


FIG. 1.— Images of the magnetic field $B_z(G)$, streamlines, deformation (S) and vortical (Ω) Eulerian coherent structures, and Q -criterion at: 12-Dec-2006 14:24 UT, 12-Dec-2006 18:24 UT, 12-Dec-2006 22:24 UT, 13-Dec-2006 02:24 UT (from top to bottom).

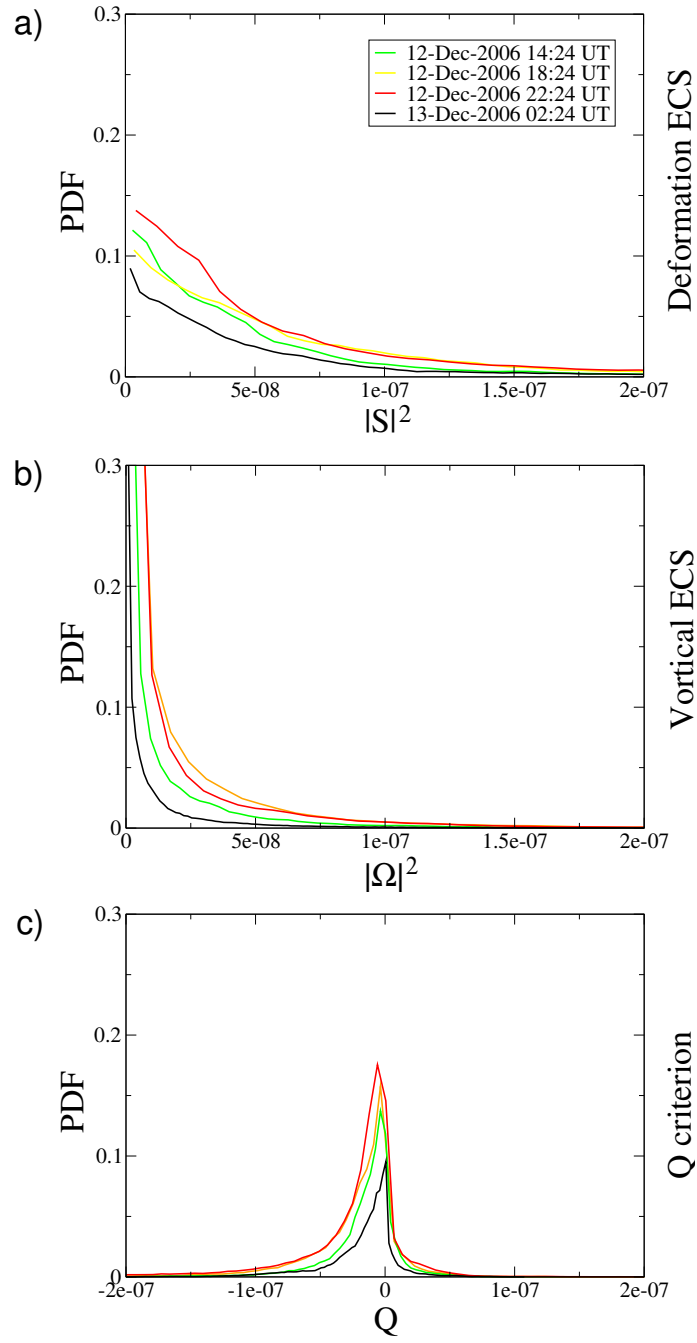


FIG. 2.— PDF of Eulerian coherent structures (ECS) as a function of: (a) $|S|^2$, (b) $|\Omega|^2$, (c) Q-criterion; at 12-Dec-2006 14:24 UT (green), 12-Dec-2006 18:24 UT (yellow), 12-Dec-2006 22:24 UT (red), 13-Dec-2006 02:24 UT (black).

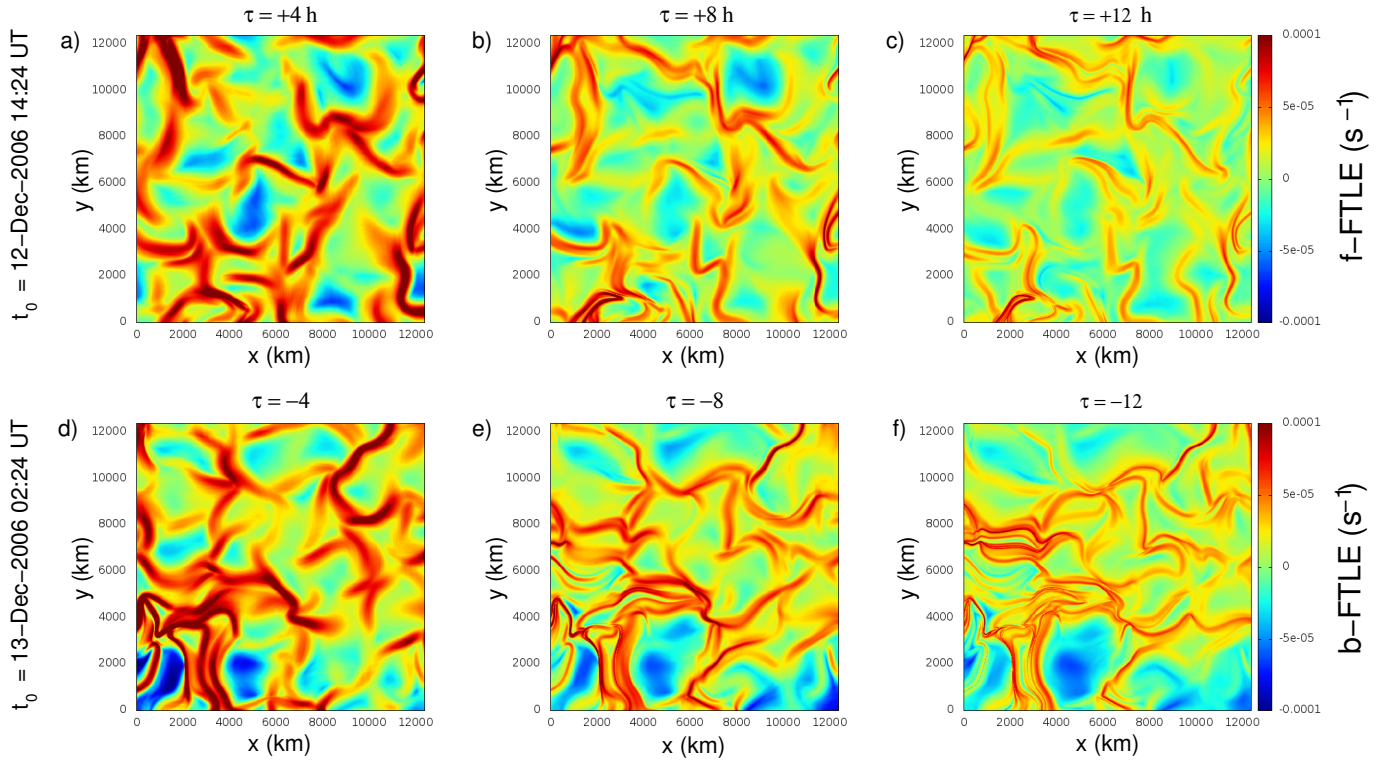


FIG. 3.— **Lagrangian coherent structures.** Upper panel: f-FTLE for t_0 at 12-Dec-2006 14:24 UT with (a) $\tau = +4$ hr, (b) $\tau = +8$ hr, (c) $\tau = +12$ hr. Bottom panel: b-FTLE for t_0 at 13-Dec-2006 02:24 UT with (d) $\tau = -4$ hr, (e) $\tau = -8$ hr, (f) $\tau = -12$ hr.

Attracting and repelling LCS

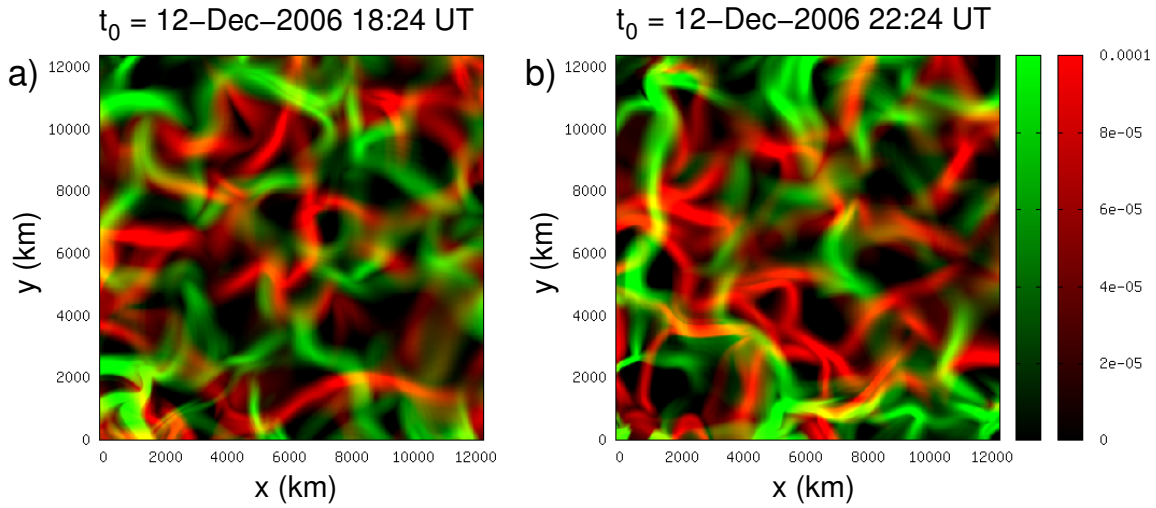


FIG. 4.— **Attracting and repelling Lagrangian coherent structures** given respectively by the b-FTLE (s^{-1}) (red) and f-FTLE (s^{-1}) (green) at (a) 12-Dec-2006 18:24 UT, (b) 12-Dec-2006 22:24 UT.

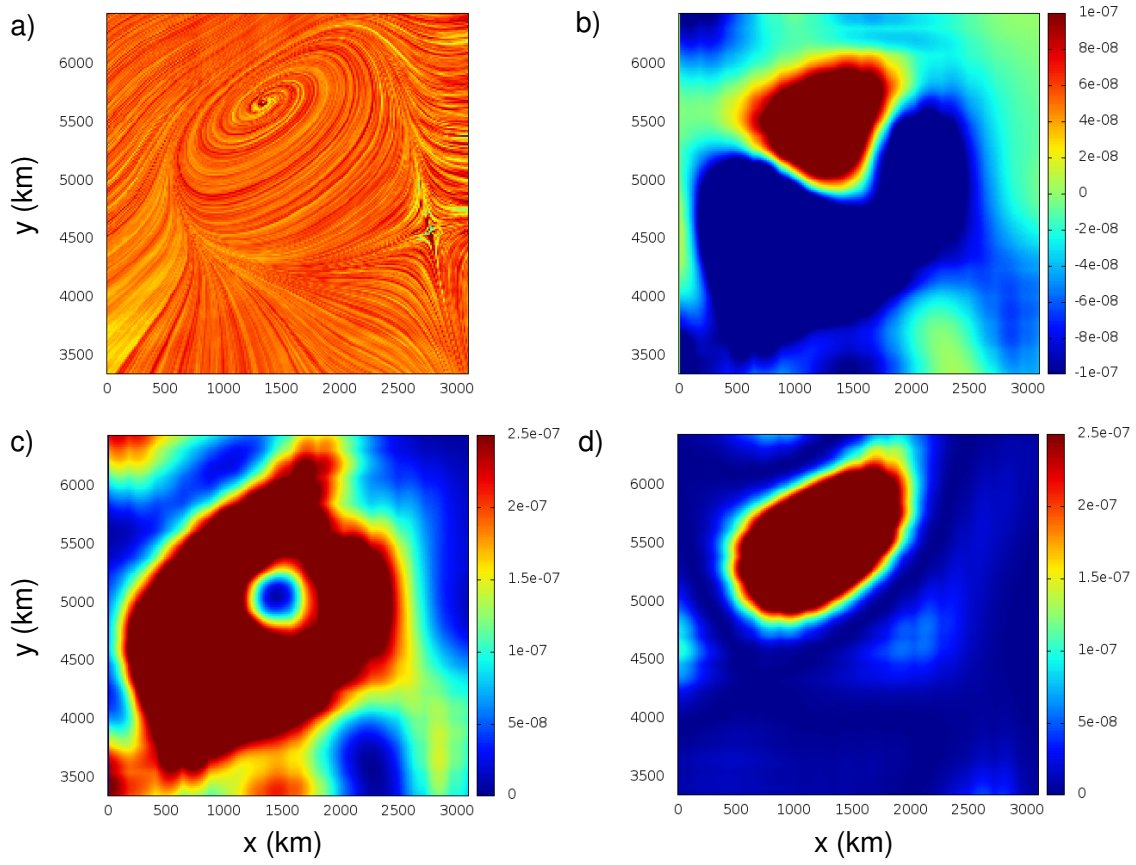


FIG. 5.— **Enlargement of the rectangle region indicated at Figure 1 at 12-Dec-2006 18:24 UT:** (a) streamlines, (b) Q-criterion, (c) $|\Omega|^2$, (d) $|S|^2$.

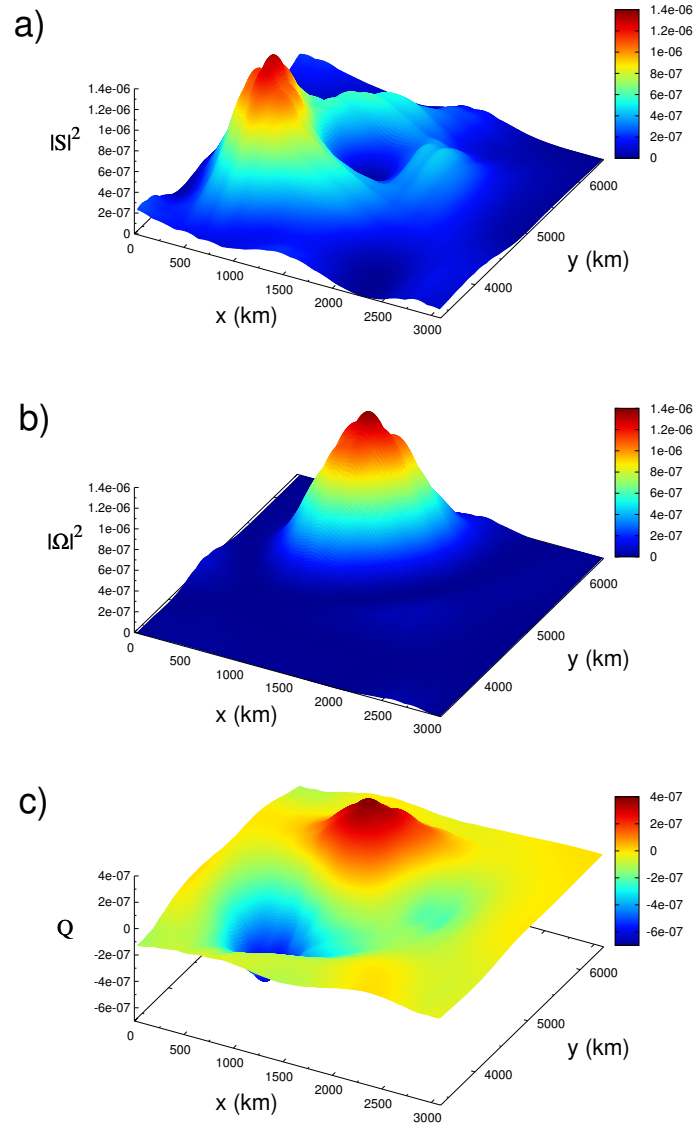


FIG. 6.— 3D plots of Eulerian coherent structures as a function of (x, y) , corresponding to Figure 5. (a) $|S|^2$, (b) $|\Omega|^2$ and (c) Q-criterion.

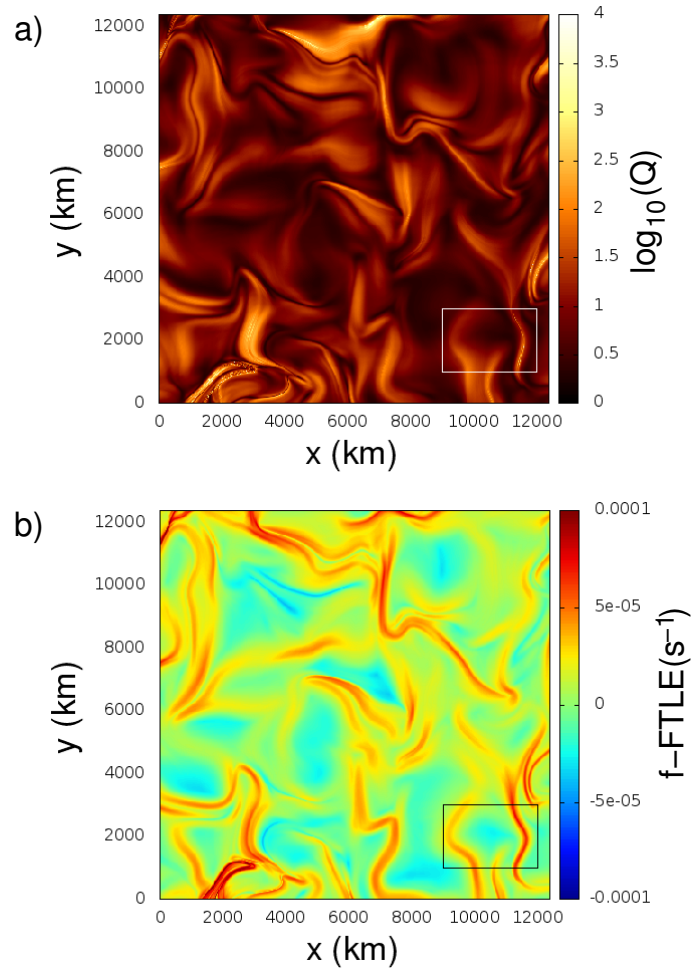


FIG. 7.— Comparison of the squashing Q -factor and repelling LCS. (a) Intensity plot of $\log_{10}(Q)$; (b) the $f\text{-FTLE}$ for $t_0 = 12\text{-Dec-2006 } 14:24 \text{ UT}$ and $\tau = +12 \text{ h}$.

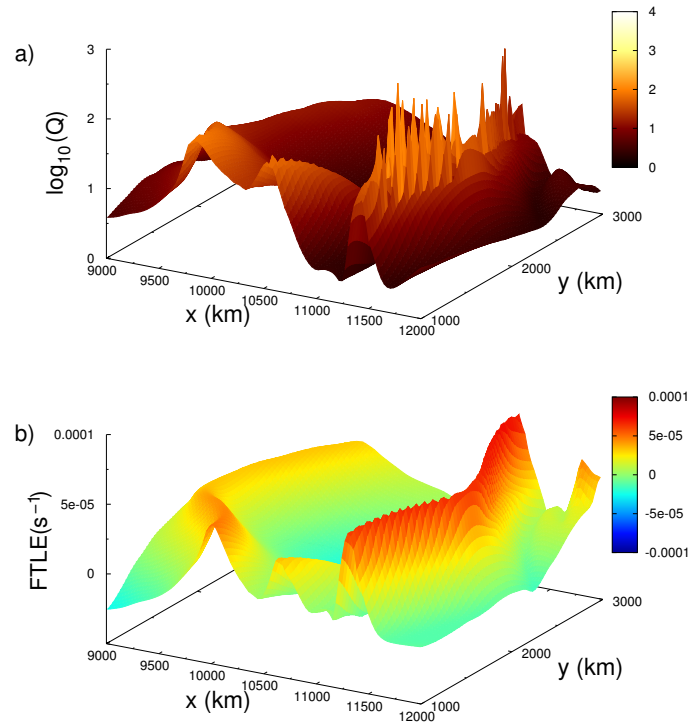


FIG. 8.— **3D plots of the squashing Q-factor and repelling LCS.** (a) $\log_{10}(Q)$; (b) the f-FTLE for $t_0 = 12\text{-Dec-2006 } 14:24 \text{ UT}$ and $\tau = +12 \text{ h}$, corresponding to the rectangle regions indicated in Fig. 7.

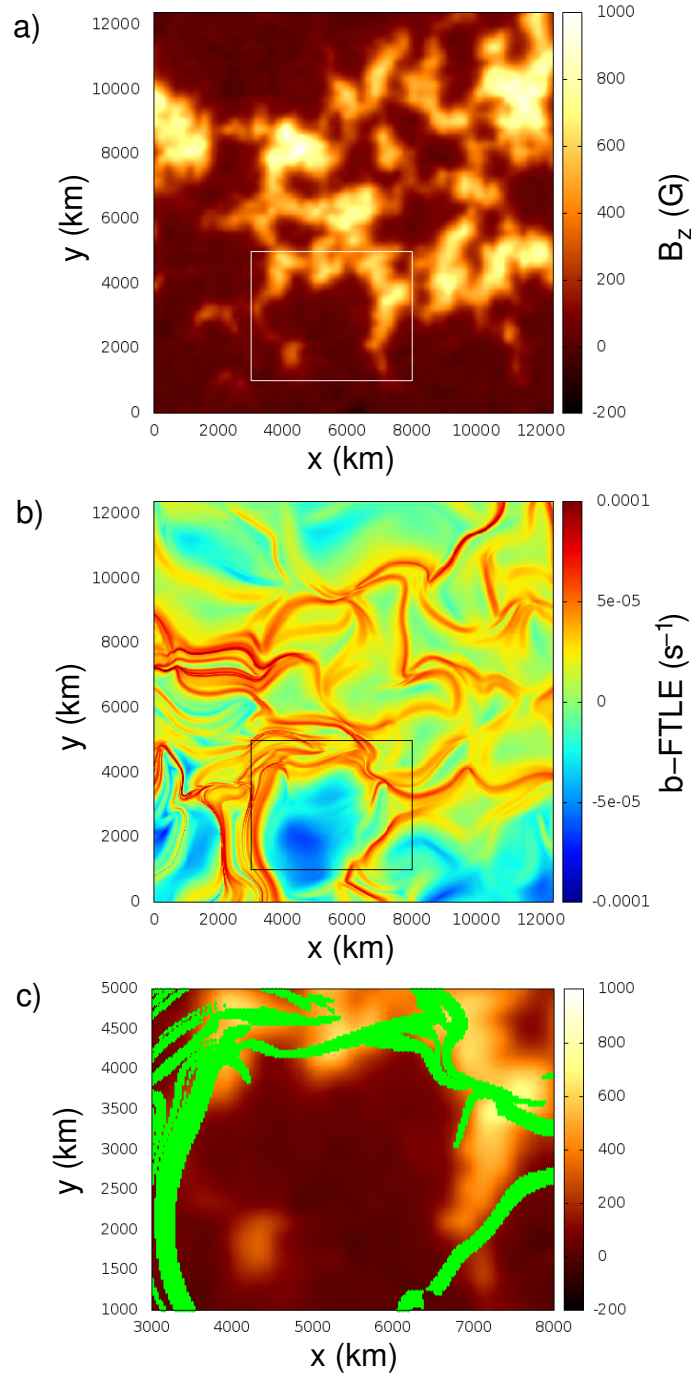


FIG. 9.— **Comparison of the magnetic field and attracting LCS.** (a) The line-of-sight magnetic field B at $t = 13\text{-Dec-2006 } 02:24$ UT and (b) the b-FTLE for $t_0 = 13\text{-Dec-2006 } 02:24$ UT and $\tau = -12$ h. A superposition of the rectangle regions of (a) and (b) (green) is shown in (c), where the thresholded $\sigma_1 > 4 \times 10^{-5}$ is applied to b-FTLE.

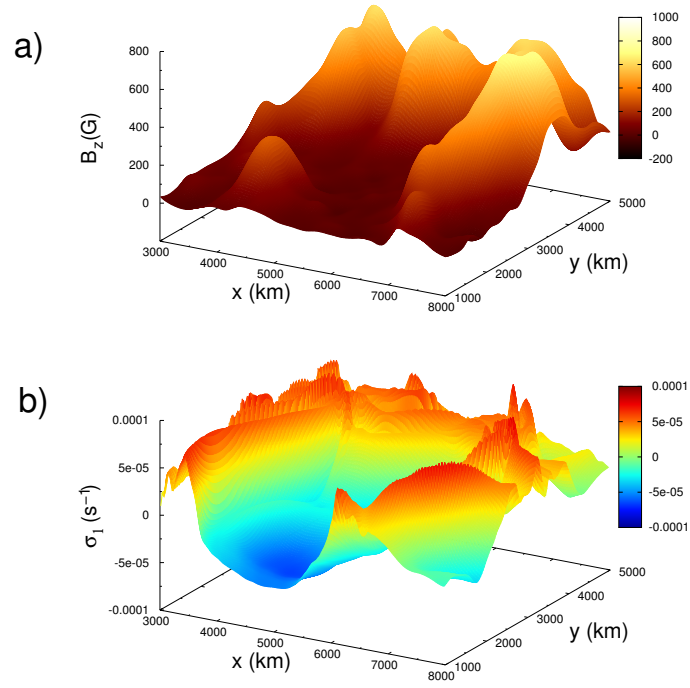


FIG. 10.— **3D plots showing the comparison of the magnetic field and attracting LCS.** (a) The line-of-sight magnetic field B_z at $t=13\text{-Dec-2006 } 02:24$ UT and (b) the b-FTLE for $t_0 = 13\text{-Dec-2006 } 02:24$ UT and $\tau = -12$ h, corresponding to the rectangle regions indicated in Figs. 9(a)-(b).

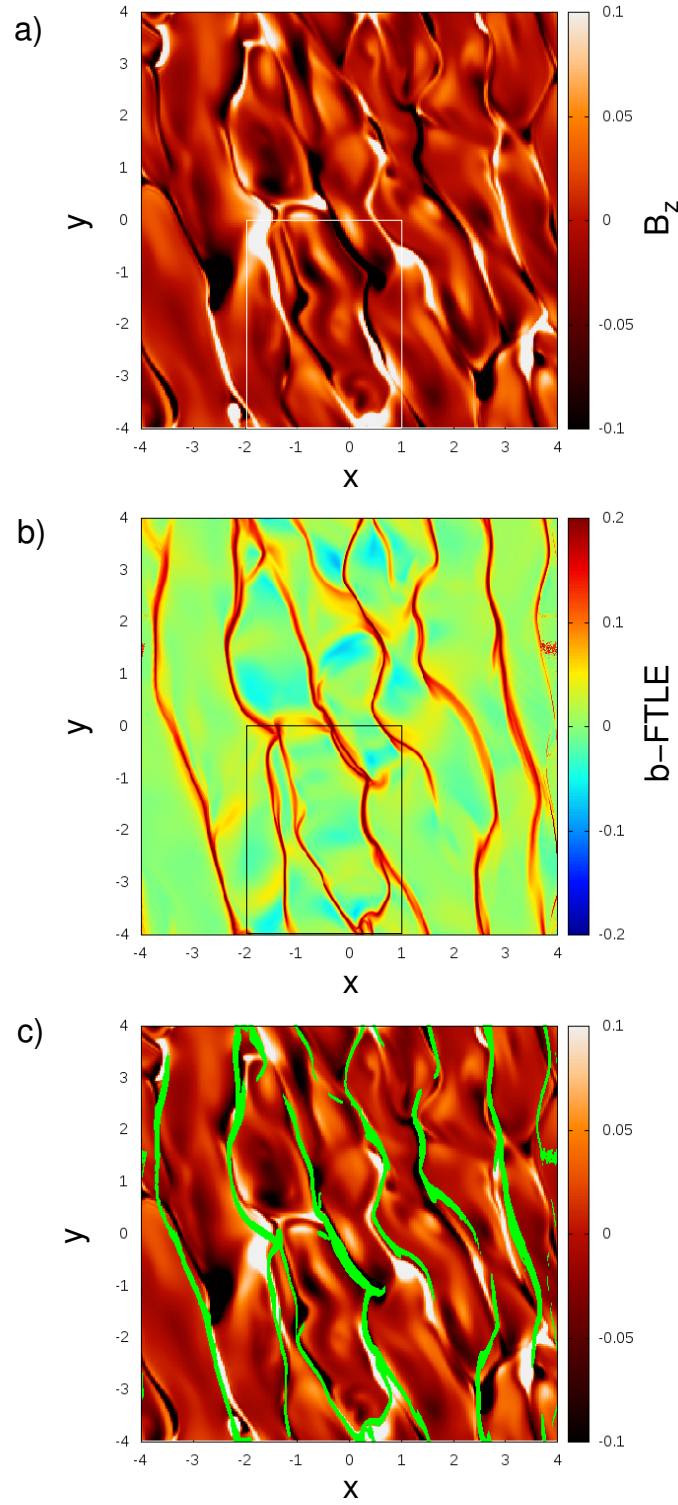


FIG. 11.— **2D plots of numerical simulation of compressible convection.** (a) The vertical component of the magnetic field B_z at time t_0 ; (b) the b-FTLE computed at t_0 with $\tau = -10$ time units; (c) a superposition of (a) and (b) (green), where the threshold $\sigma_1 > 0.1$ is applied to b-FTLE.

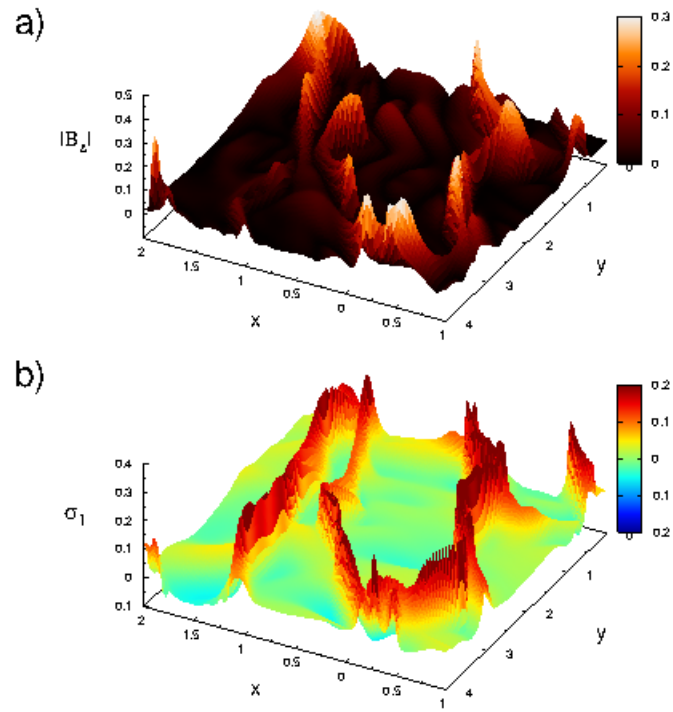


FIG. 12.— 3D plots of numerical simulation of compressible convection corresponding to the rectangle regions indicated in Figs. 9(a)-(b). (a) Modulus of the vertical component of the magnetic field B_z at time t_0 ; (b) the b-FTE for t_0 and $\tau = -10$ time units.